Brush-Like Cobalt Nitride Anchored Carbon Nanofiber Membrane: Current Collector-Catalyst Integrated Cathode for Long Cycle Li–O2 Batteries

Ki Ro Yoon,[†] Kihyun Shin,[†] Jiwon Park,[‡,§] Su-Ho Cho,[†] Chanhoon Kim,[†] Ji-Won Jung,[†] Jun Young Cheong,[†] Hye Ryung Byon,[‡,§] Hyuk Mo Lee,*,[†] and Il-Doo Kim*,[†]

[†]Department of Materials Science and Engineering, Korea Advanced Institute of Science and Technology (KAIST), 291 Daehak-ro, Yuseong-gu, Daejeon 34141, Republic of Korea

[‡]Department of Chemistry, Korea Advanced Institute of Science and Technology (KAIST), 291 Daehak-ro, Yuseong-gu, Daejeon 34141, Republic of Korea

[§]KAIST Institute NanoCentury, 291 Daehak-ro, Yuseong-gu, Daejeon 34141, Republic of Korea

Ⓢ Supporting Information

ABSTRACT: To achieve a high reversibility and long cycle life for lithium–oxygen (Li−O2) batteries, the irreversible formation of Li2O2, inevitable side reactions, and poor charge transport at the cathode interfaces should be overcome. Here, we report a rational design of air cathode using a cobalt nitride (Co4N) functionalized carbon nanofiber (CNF) membrane as current collector-catalyst integrated air cathode. Brush-like Co4N nanorods are uniformly anchored on conductive electrospun CNF papers via hydrothermal growth of Co(OH)F nanorods followed by nitridation step. Co4N-decorated CNF (Co4N/CNF) cathode exhibited excellent electrochemical performance with outstanding stability for over 177 cycles in Li−O2 cells. During cycling, metallic Co4N nanorods provide sufficient accessible reaction sites as well as facile electron transport pathway throughout the continuously networked CNF. Furthermore, thin oxide layer (<10 nm) formed on the surface of Co4N nanorods promote reversible formation/decomposition of film-type Li2O2, leading to significant reduction in overpotential gap (∼1.23 V at 700 mAh g^{-1}). Moreover, pouch-type Li-air cells using Co4N/CNF cathode stably operated in real air atmosphere even under 180° bending. The results demonstrate that the favorable formation/decomposition of reaction products and mediation of side reactions are hugely governed by the suitable surface chemistry and tailored structure of cathode materials, which are essential for real Li−air battery applications.

KEYWORDS: cobalt nitrides, carbon nanofibers, lithium−oxygen batteries, flexible, air cathodes
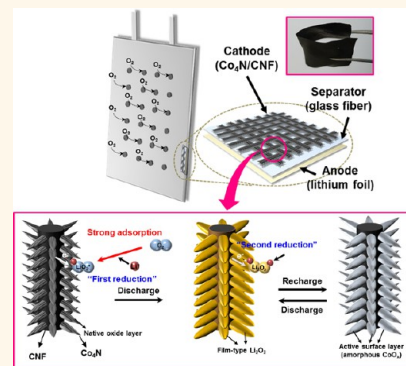
The nonaqueous lithium−oxygen (Li−O2) batteries based on reversible formation of lithium peroxide (Li2O2) possess significantly higher theoretical energy density (∼3500 Wh kg^{-1}) compared to conventional Li-ion batteries (<200 Wh kg^{-1}),[1] thus have been considered as a potential alternative for transporting electric vehicles.[2] However, implementing Li−O2 batteries into our daily life is still a big challenge because the solid Li2O2 that accumulates on the pores of cathodes during discharge causes a significant polarization loss during charge process and poor cycle life.[3,4] Therefore, various oxide materials including transition metal oxides, perovskite or spinel oxides, and their composites have been employed in cathodes as catalysts for improving the Li−O2 cell performance.[5,6] Among them, cobalt oxide has received ever-growing interest as a promising electrocatalyst due to its low-cost, earth abundance, and decent catalytic activities toward oxygen reduction and evolution reactions (ORR/OER).[7−9] However, cobalt oxide based electrodes have suffered from the poor electronic conductivity owing to their p-type semiconducting nature, resulting in low catalytic performance far below the expectation.[10,11]

More recently, metal oxynitrides and metal nitrides also have been studied to overcome intrinsic limitation of metal oxide catalysts stemmed from poor electrical conductivity.[12−14] Since electronic energy state level of N 2p orbitals in nitride materials
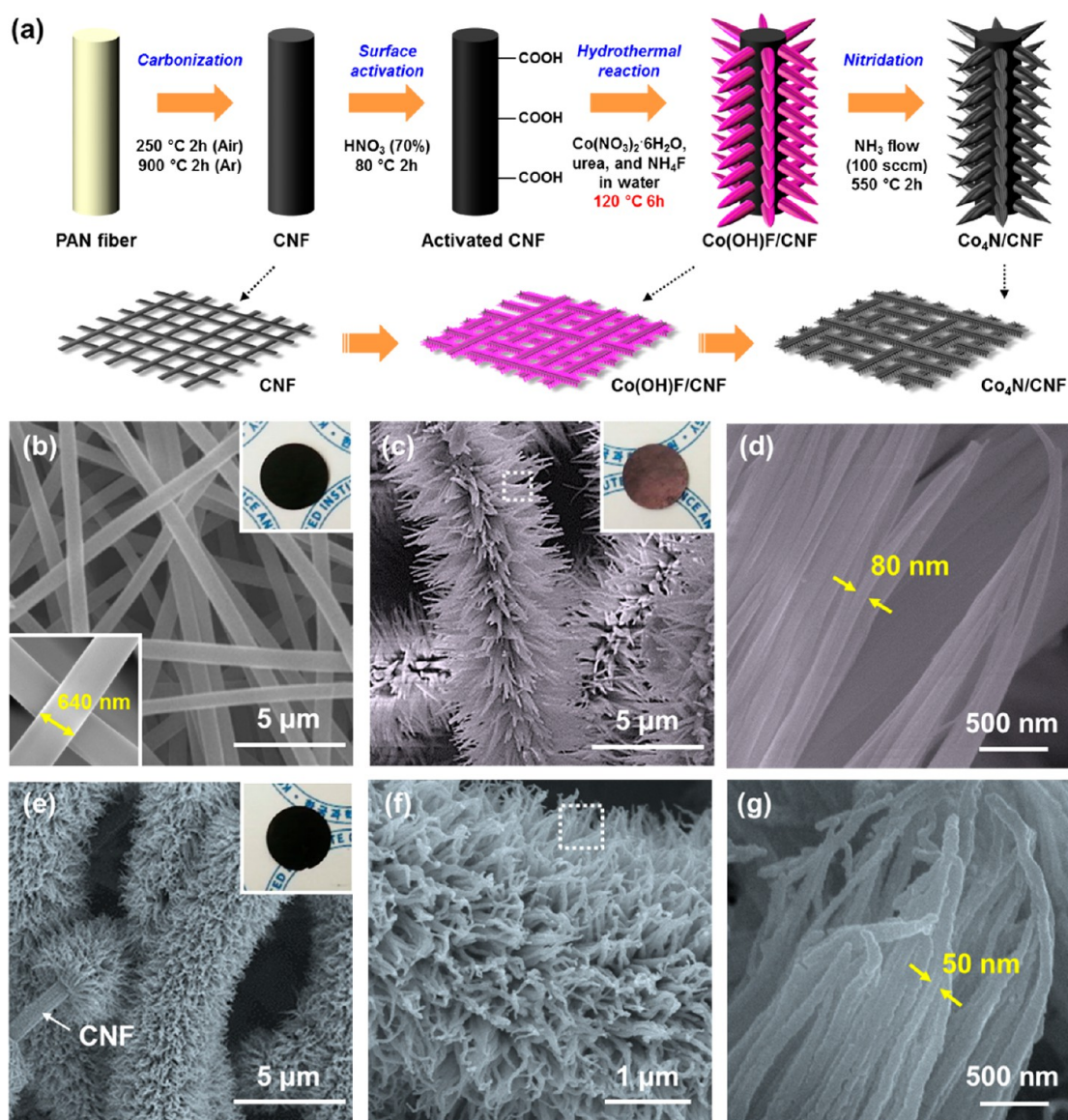
Figure 1. (a) Schematic images of Co₄N/CNF fabrication procedure; SEM images and photograph images (insets) of (b) CNF, (c,d) Co(OH)F/CNF, and (e,f,g) Co₄N/CNF with different magnifications. The permission to use the logo in print or digital formats was granted from KAIST.

is higher than that of O 2p orbitals, N-doped metal oxides can have high electronic conductivities by lowering band gap or overlapping of conduction and valence bands. Thus, far, various nitride materials including titanium nitride,[15,16] molybdenum nitride,[17] nickel nitride,[18] cobalt nitride,[19,20] nickel−iron nitride,[21] and cobalt−molybdenum nitride,[22,23] have been suggested for applications in the energy conversion and storage devices. Among them, particular interests are focused on cobalt nitrides since various nitride compounds, *i.e.*, Co_2N, Co_3N, and Co_4N, could be existed due to the electron delocalization modulation.[24,25] Especially, the metallic Co_4N catalyst exhibits high stability and outstanding OER activity in alkaline solution due to the formation of thin oxide layer on Co_4N, which can facilitate the electrocatalysis as well as fast interfacial charge transfer. Nonetheless, these characteristic features of Co_4N have never been investigated in nonaqueous Li−O₂ batteries.

Meanwhile, conductive agents (*e.g.*, Ketjen black, Super P, graphene, and carbon nanotubes) and polymeric binders (*e.g.*, polyvinylidene fluoride and polytetrafluoroethylene) are commonly incorporated in conventional air cathodes,[26−28] but detrimental reactivity of carbonaceous electrode via reaction of Li_2O_2 with carbon[29] and irreversible side reactions induced by decomposition of polymeric binder have become critical issues.[30,31] Furthermore, electrode materials including these additives are usually slurry-casted onto heavy metal meshes/foams or porous carbon papers, which hugely increase the total weight of the cathodes in the fixed volume of the Li−O₂ cells.[5,6,32] Therefore, rational design of air cathodes involving binder-free, ultralight weight, high conductivity, and catalytic activity is indispensable to overcome the aforementioned issues.

In this study, we introduce brush-like metallic Co_4N nanorods anchored N-doped carbon nanofiber (CNF) membrane (hereafter, Co_4N/CNF) as a free-standing and ultralight air cathode, which are synthesized via a hydrothermal coating of cobalt fluoride hydroxide (Co(OH)F) on CNF (Co(OH)F/CNF) and subsequent nitridation annealing. The strong adsorption energy of LiO_2 (ranging from −3.613 to
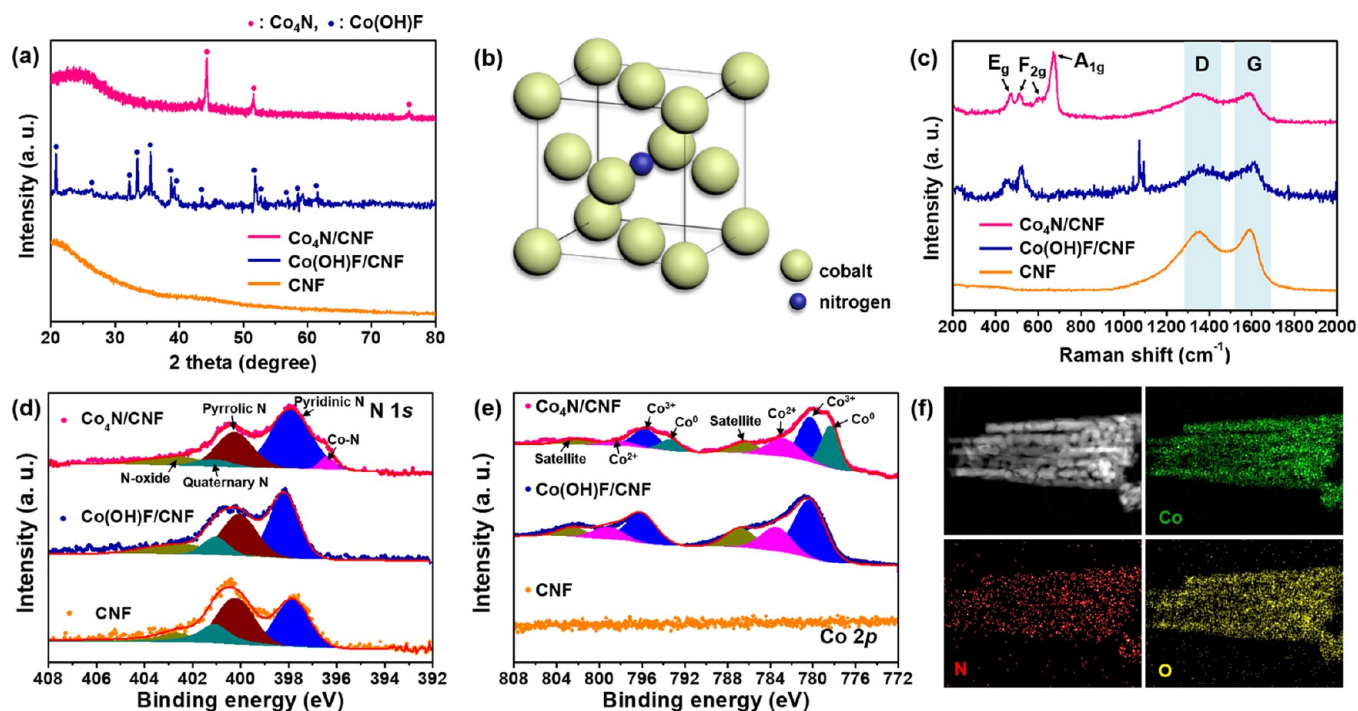
Figure 2. (a) XRD results of CNF, Co(OH)F/CNF, and Co$_4$N/CNF; (b) crystallographic structure of Co$_4$N; (c) Raman spectra, XPS spectra in (d) N 1s and (e) Co 2p regions for CNF, Co(OH)F/CNF, and Co$_4$N/CNF; and (f) STEM image of Co$_4$N and its EDS elemental mapping (Co, N, and O).

−8.145 eV) on the Co$_4$N nanorods promotes the film-type Li$_2$O$_2$ growth during discharge reaction, but naturally formed, catalytically active oxide film (<10 nm) on Co$_4$N can efficiently mediate reaction products during charge process, resulting in long-term cyclability for over 177 cycles without severe discharge−charge polarization. The excellent electrochemical performance of Li−O$_2$ cell using Co$_4$N/CNF electrode in this work was compared with other reported Co-based catalysts (Table S1). Finally, the Co$_4$N/CNF cathode is assembled into pouch-type Li−air cells, demonstrating an outstanding reversibility and robust flexibility even in real air atmosphere.

RESULTS AND DISCUSSION

Morphological Features. Synthetic process and microstructural evolution of the CNF, Co(OH)F/CNF, and Co$_4$N/CNF were presented in Figure 1. As a first step to fabricate the CNF paper, one-dimensional (1D) nanofibrous polymer matrix was obtained from polyacrylonitrile (PAN) dissolved dimethylformamide (DMF) solution via conventional electrospinning method.[33] Figure S1 displays photograph and scanning electron microscopy (SEM) images of as-spun and stabilized PAN fibers. White colored as-spun fiber mat consisted of randomly entangled nonwoven fibers was turned into dark brown mat after oxidation at 250 °C for 2 h, resulting from the transformation of nitrile group (−C≡N) of PAN to cyclized ladder structure which has high thermal stability.[34] Stabilized PAN fibers were then carbonized at 900 °C in Ar-filled tube furnace, and dark colored CNF paper was obtained (Figure 1b inset). Different from the conventional current collectors, such as carbon papers or metal meshes/foams (Table S2), PAN-driven CNF paper has an ultralight weight (0.9 ± 0.2 mg cm^{-1}) and a large surface area with numerous void spaces due to the thin membrane thickness (∼100 μm)

and nature of nanoscale fibrils with an average diameter of ∼640 nm (Figure 1b).

The PAN-driven CNF initially has hydrophobic surface,[35] so metal oxides/hydroxides could be hardly seeded or easily detached from the CNF during the hydrothermal reaction (Figure S2). So, the surface of CNF paper was activated by dipping in 70% nitric acid (HNO$_3$) solution for 2 h. Consequently, the amount of polar functional groups, i.e., carboxyl group (O−C=O), which give hydrophilicity to the outer surface of CNF, evidently increased (Figure S3). After that, the HNO$_3$ treated (activated) CNF was kept at 120 °C for 6 h in an autoclave with aqueous solution employing various additives (Co(NO$_3$)$_2$·6H$_2$O, urea, and NH$_4$F) for hydrothermal growth of nanorods.[24,25] Consequently, purple colored brush-like Co(OH)F overlayers were uniformly grown on the surface of CNF (Figure 1c). The brush-like Co(OH)F consists of a bundle of long nanorods with an average diameter of ∼80 nm (Figure 1d). To obtain Co$_4$N/CNF, we carried out the nitridation at 550 °C for 2 h with ammonia (NH$_3$) gas flow (100 sccm), that condition (nitridation temperature, duration time, and flow rate of NH$_3$ gas) was carefully optimized via various control tests (Figure S4). The phase transformation from Co(OH)F to Co$_4$N in the presence of NH$_3$ gas occurs via the following equation:[25]

$$24Co(OH)F + 40NH_3$$
$$\rightarrow 6Co_4N + 24H_2O + 5N_2 + 24NH_4F \qquad (1)$$
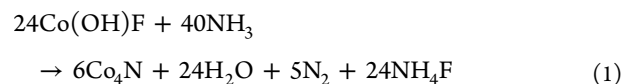
As displayed in Figure 1e, the overall brush-like structure was similarly maintained after nitridation step. In detail, dozens of Co$_4$N nanorods that have an average diameter of ∼50 nm and length of 2−5 μm were densely assembled along the trace of CNF to form brush-like Co$_4$N/CNF (Figure 1f,g). These distinctive morphological features are considered to have some
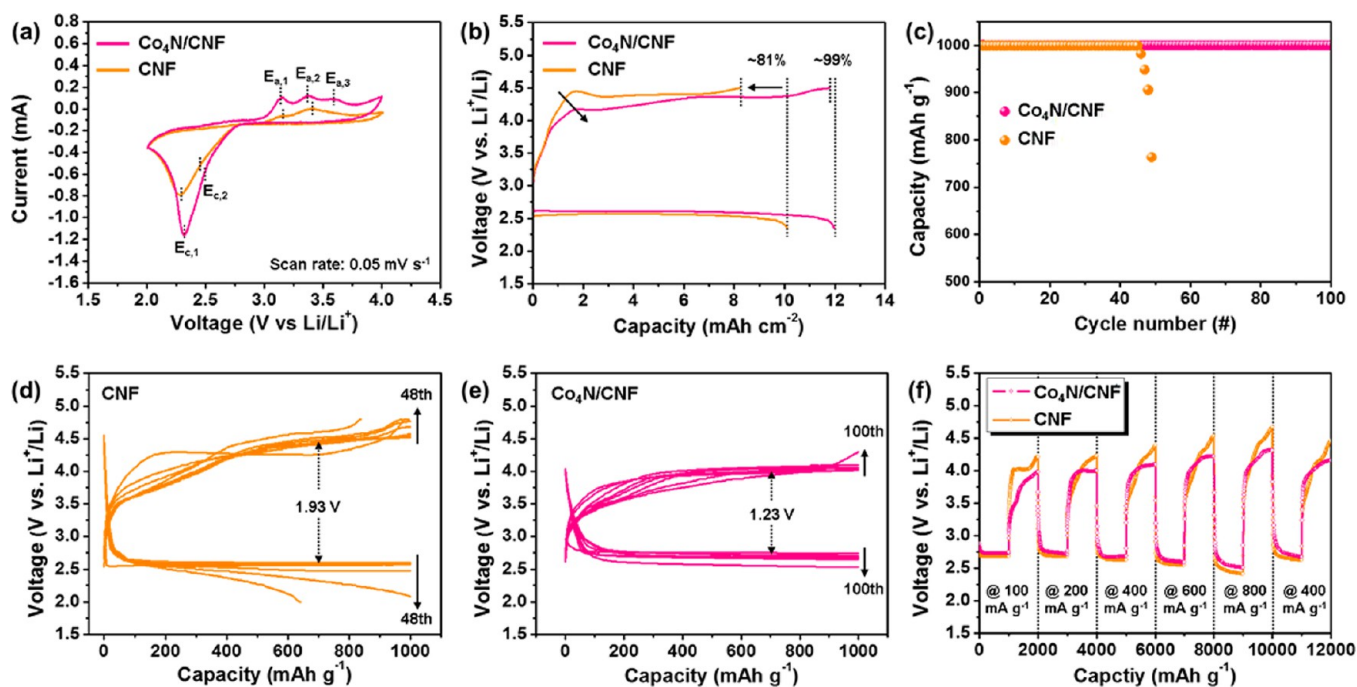
Figure 3. (a) CV curves with a scan rate of 0.05 mV s^{-1}; (b) initial discharge/charge profiles (voltage: 2.35−4.5 V); (c) cycling performance of CNF and Co$_4$N/CNF electrodes with a capacity restriction (1000 mAh g^{-1}), and corresponding discharge/charge profiles of (d) CNF and (e) Co$_4$N/CNF electrodes (voltage: 2−4.8 V); and (f) rate capability of CNF and Co$_4$N/CNF electrodes in Li−O$_2$ cells.

advantages for air cathode in Li−O$_2$ cells: (i) efficient charge transport due to the intimate electrical contact between Co$_4$N nanorods and underneath CNF without the use of polymeric binder, and (ii) numerous electrochemical reaction sites due to the mesopores in-between nanorods and macropores in-between the bundles of nanorods.

Phase Information and Structural Features. The crystalline phases of prepared samples were investigated by analyzing X-ray diffraction (XRD) pattern (Figure 2a). Pristine CNF shows broad peak at around 23°, which is attributed to (002) planes of turbostratic carbon structure (d_{002}= 0.38 nm) as observed by transmission electron microscopy (TEM) (Figure S5).[35] In the diffraction pattern of Co(OH)F/CNF, the majority peaks indexed with blue circles are well matched with Co(OH)F phase (JCPDF#50-0827). After nitridation of Co(OH)F/CNF, well crystallized face-centered cubic (FCC) phase was observed in Co$_4$N/CNF, which is consistent with the previously reported results.[24,36] As depicted in Figure 2b, Co atoms are packed in the FCC arrangement with preferred (111) orientation (44.2° in diffraction pattern of Co$_4$N) and N atom is placed at the middle of the unit cell. For a comparison purpose, cobalt oxide anchored CNF membrane (CoO$_x$/CNF) was also prepared in the same annealing process (550 °C, 2 h) except for NH$_3$ gas flow. As shown in Figure S6, the morphology of CoO$_x$/CNF is similar to that of Co$_4$N/CNF, but its crystalline phases are composed of both CoO and Co$_3$O$_4$.

Raman spectrum of pristine CNF indicates that two identical peaks occurred at 1359 and 1590 cm^{-1}, which are related to the D and G bands of graphite, respectively (Figure 2c).[37] In Co(OH)F/CNF, vibration modes of Co elements, such as E_g (478 cm^{-1}) and F_{2g} (517 and 618 cm^{-1}), were observed.[38,39] Additional peaks between 1080 and 1120 cm^{-1} might be attributed to the organic residue components, such as urea or NH$_4$F, because these peaks clearly disappeared after high

temperature nitridation process. In Co$_4$N/CNF, A$_{1g}$ (687 cm^{-1}) vibration mode of Co elements appeared, and D and G bands from graphitic carbons also maintained.

In order to investigate the changes of chemical bonding states, X-ray photoelectron spectroscopy (XPS) analysis for CNF, Co(OH)F/CNF, and Co$_4$N/CNF was carried out. As presented in Figure 2d, pristine CNF has natively doped N atoms at various sites including pyridinic N (398.1 eV), pyrrolic N (400.2 eV), quaternary N (401.3 eV), and N-oxide (402.8 eV),[40,41] resulting from the pyrolysis of −C≡N group of PAN.[35] These native N dopants in CNF might be beneficial to enhance the electrochemical reactivity especially toward ORR and the electronic conductivity (see details in Figure S3).[42−44] All peaks in N 1s region were similarly maintained after hydrothermal reaction, but, a new peak at 396.2 eV was observed in Co$_4$N/CNF, which is originated from the strong Co−N bonds formed after nitridation process.[18,45] To investigate the reactivity between NH$_3$ and CNF during nitridation, we compared XPS spectra of pristine CNF and NH$_3$ treated CNF. As shown in Figure S7 and Table S3, the amount of N 1s and C−N bonds in C 1s (285.8 eV) slightly increased (from 5.54 to 5.79 at% and from 4.52 to 7.76 at%, respectively) after NH$_3$ treatment, suggesting small portion of nitrogen can be incorporated into CNF matrix. The sheet resistance of CNF mat also decreased (from 50.8 to 45.2 Ω sq^{-1}), which is beneficial for enhancing charge transport of CNF as a current collector.

In Co 2p spectra (Figure 2e), Co^{3+} (780.1 eV) and Co^{2+} (783 eV) peaks with satellites (786.2 eV) were detected after hydrothermal process, which come from Co(OH)F.[25] Co^0 peak (778.4 eV) was evidently detected in Co$_4$N/CNF, because Co$_4$N has a similar atomic structure with closely packed metallic cobalt, but having slightly longer Co−Co distance due to the N at the middle of unit cell (Figure 2b).[36] The Co^{3+} and Co^{2+} peaks were still observed in Co$_4$N/CNF, suggesting that
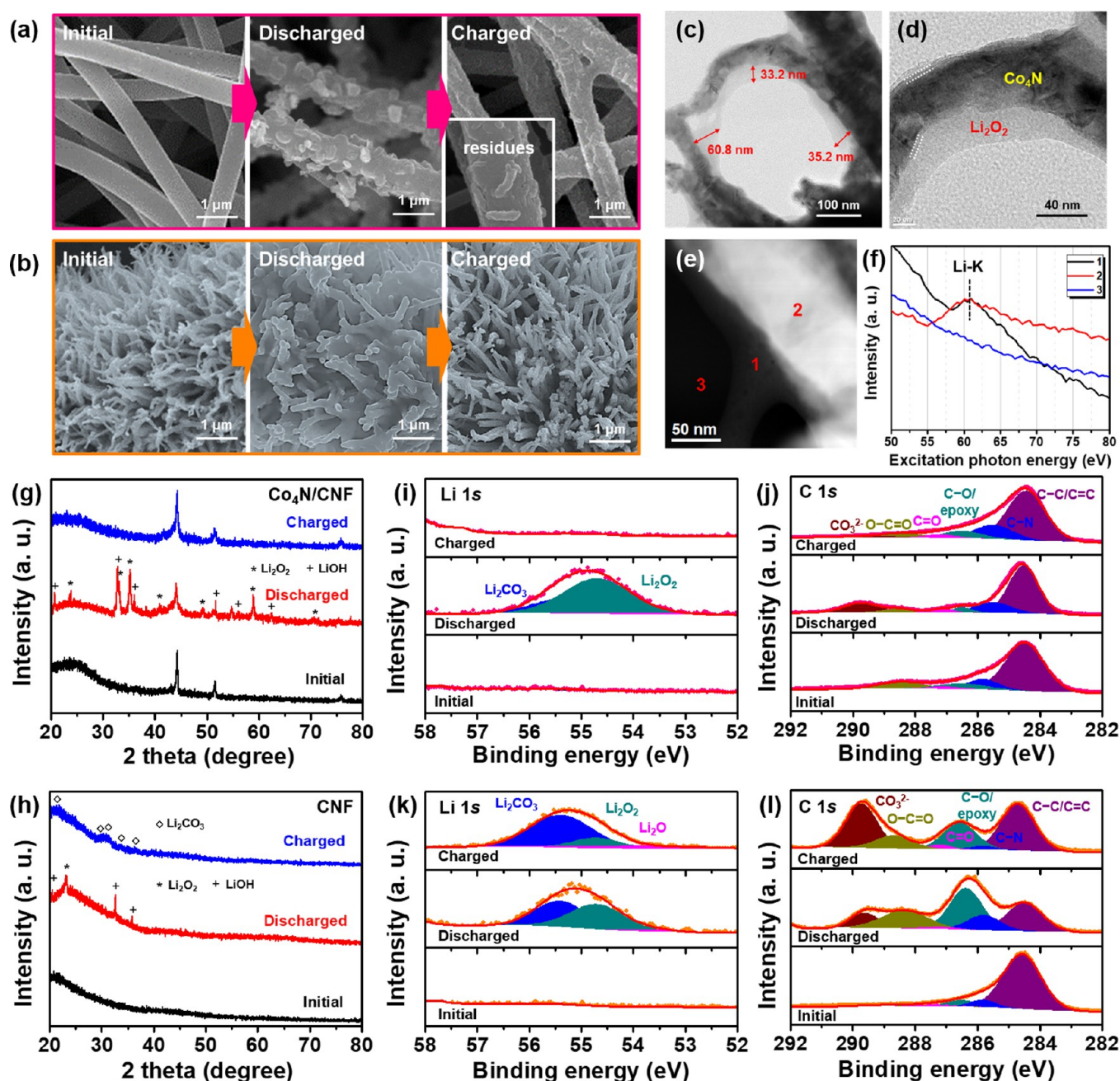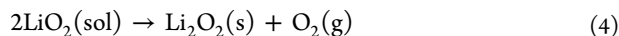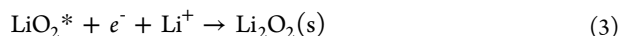
Figure 4. *Ex situ* SEM images of (a) CNF and (b) Co_4N/CNF electrodes at initial, discharged, and charged states with current densities of 200 mA g^{-1} and depth of discharge/charge capacities of 1000 mAh g^{-1}; (c, d) TEM images, (e) STEM image, and (f) corresponding EELS spectra of discharged Co_4N/CNF; *ex situ* XRD spectra of (g) Co_4N/CNF and (h) CNF electrodes at initial, discharged, and charged states; *ex situ* XPS spectra of initial, discharged, and charged Co_4N/CNF electrodes in (i) Li 1s and (j) C 1s regions and those of CNF electrodes in (k) Li 1s and (l) C 1s regions.

the surface of Co_4N has been partially oxidized into cobalt oxide that was not identified by TEM observation (Figure S8). From energy-dispersive X-ray spectroscopy (EDS) mapping (Figure 2f), we confirmed that native oxide as well as Co and N atoms in Co_4N are detected along with the nanorods. In Figure S9, the surface resistance of Co_4N/CNF (389.1 Ω) is higher than that of pristine CNF (81.3 Ω) due to the polycrystalline nature and porous morphologies of Co_4N nanorods, but it is much lower than that of CoO_x/CNF (2777.8 Ω). Even though the electrochemical reactions are mainly governed by the charge transfer at the interfaces of electrode materials/electrolyte or solid reaction products, the enhanced surface

electrical property of Co_4N/CNF would be beneficial for overall cell operation compared with CoO_x/CNF.

Electrochemical Properties. To investigate the potential feasibility of Co_4N/CNF as a free-standing air cathode, we characterized the electrochemical properties using Swagelok-type cells composed of a lithium metal anode, electrolyte (1 M LiTFSI dissolved TEGDME) impregnated into a glass fiber separator, and CNF, Co_4N/CNF or CoO_x/CNF electrodes as air cathodes without the conventional current collectors. Cyclic voltammograms (CVs) for CNF and Co_4N/CNF electrodes in Li−O_2 cells were recorded after 3 h-O_2 purging (Figure 3a). Several peaks appeared in both cathodic and anodic regions,

which were closely related to the formation and decomposition of Li_2O_2 during discharge and charge processes. In many previous studies, the stepwise formations of Li_2O_2 have been proposed as expressed in following equations:

$$O_2(g) + e^- + Li^+ \rightarrow LiO_2 \tag{2}$$

$$LiO_2^* + e^- + Li^+ \rightarrow Li_2O_2(s) \tag{3}$$

$$2LiO_2(sol) \rightarrow Li_2O_2(s) + O_2(g) \tag{4}$$

During the discharge process, reduced oxygen ions (O_2^-) are adsorbed at the cathode surface to form superoxide species (LiO_2) (eq 2, the peak appeared at ~2.5 V ($E_{c,2}$)), and adsorbed LiO_2 (LiO_2^*) are second reduced to form film-type (<10 nm) Li_2O_2 (eq 3, the peak appeared at ~2.3 V ($E_{c,1}$)), so-called surface-adsorption pathway. Otherwise, two solvated superoxide species, *i.e.*, LiO_2(sol), are chemically disproportionated into Li_2O_2 as toroidal crystals and gaseous O_2 in the solution by solvation-mediated pathway (eq 4).[46−48] Here, the positively shifted $E_{c,1}$ and $E_{c,2}$ peaks and the increased current of Co_4N/CNF in comparison with those of CNF imply that Co_4N/CNF electrode has better ORR properties than pristine CNF electrode.

The decomposition of Li_2O_2 takes place during charging by following equations:

$$Li_{2-x}O_2(s) \rightarrow (1-x)Li^+ + (1-x)e^- + LiO_2 \tag{5}$$

$$Li_2O_2(s) \rightarrow Li^+ + e^- + LiO_2(sol) \tag{6}$$

$$Li_2O_2(s) \rightarrow 2Li^+ + 2e^- + O_2(g) \tag{7}$$
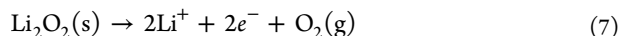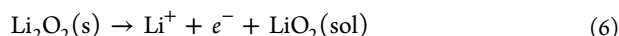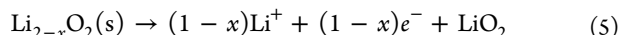
The obvious peaks at ~3.1 V ($E_{a,1}$) in anodic scan for both samples are originated from the amicable decomposition of nonstoichiometric $Li_{2-x}O_2$ especially at the outer part of Li_2O_2 (eq 5).[49] The second peaks at ~3.3 V ($E_{a,2}$) can be assigned to the oxidation at the main part of Li_2O_2, mainly formed by solvation-mediated discharge process, through one electron transfer (eq 6).[48] The additional peak at higher potential (~3.7 V, $E_{a,3}$) was observed in Co_4N/CNF electrode, which could be originated from the dissociation of densely formed Li_2O_2 film followed by two electron transfer (eq 7) or the other reaction products such as $LiOH$ or Li_2CO_3 requiring higher thermodynamic potentials.[50] These results suggest that the surface-adsorption and solvation-mediated pathways might be conjugated in discharge/recharge processes on Co_4N/CNF electrode, but CNF electrode mainly follows solvation-mediated pathway. It is noteworthy that considerable areal discharge capacity of 11.9 mAh cm^{-2} was shown in Co_4N/CNF electrode with almost 100% Coulombic efficiency (Figure 3b). On the contrary, CNF electrode exhibited 10.1 mAh cm^{-2} discharge capacity with 81% initial Coulombic efficiency and enlarged potential gap. The gravimetric capacity profiles based on the total electrode mass for CNF and Co_4N/CNF cathodes are also shown in Figure S10.

Cycling tests of CNF and Co_4N/CNF electrodes were conducted at a current density of 200 mA g^{-1} with a limited capacity of 1,000 mAh g^{-1} (Figure 3c−e). The superior catalytic activity of Co_4N/CNF was reflected in the decreased overpotentials and improved cycling performance compared with those of pristine CNF. The Co_4N/CNF electrode exhibited stable discharge/charge reactions for over 100 cycles with a small potential gap of ~1.23 V at 700 mAh g^{-1}, whereas pristine CNF electrode degraded just after 45 cycles with large

potential gap (~1.93 V at 700 mAh g^{-1}). In addition, Co_4N/CNF electrode delivered over 177 cycles without severe polarization when the capacity was restricted up to 500 mAh g^{-1} (Figure S11). As a comparative sample, potential gap of CoO_x/CNF electrode gradually increased from the initial value of 1.53 to 2.24 V and noticeable degradation was observed after 60 cycles (Figure S12). These results further highlight the efficacy of Co_4N as catalysts on improving reversibility of Li-O_2 cells. In addition, the Co_4N/CNF electrode exhibited reliable rate capability at different current densities (100, 200, 400, 600, and 800 mA g^{-1}) with a limited capacity value of 1,000 mAh g^{-1} in comparison with CNF electrode (Figure 3f). Interestingly, the charge potentials for CNF at the beginning is lower than that of Co_4N/CNF excluding the first discharge/charge at the lowest current density (100 mA g^{-1}), which can be explained by amicable decomposition of the particle-like Li_2O_2 through one electron transfer. However, the over-potentials of CNF rapidly increased when the charging is proceeded at all current densities. Such tendency was observed in the cycling profile of CNF electrode (Figure S13), while the charge overpotentials smoothly increased in case of Co_4N/CNF electrode.

***Ex Situ* and *In situ* Characterizations.** In order to verify the origins of electrochemical results of the cells using CNF and Co_4N/CNF cathodes, we examined various characterizations through SEM, TEM, XRD, XPS, electrochemical impedance spectroscopy (EIS) methods and online electrochemical mass spectroscopy (OEMS) analysis. Figure 4a shows the SEM images of CNF surfaces at the initial, discharged, and charged states with capacity limit of 1000 mAh g^{-1}. The smooth surface of initial CNF was passivated by granularly deposited and localized particles when the electrode was discharged with a current density of 200 mA g^{-1}. In addition, the similar shaped Li_2O_2 was still observed under the high current densities (500 and 1000 mA g^{-1}, Figure S14), suggesting the solvation-mediated Li_2O_2 growth occurred on the CNF surface. After recharging, the large particles disappeared, but some residues on the surface of CNF remained. On the other hand, film-like Li_2O_2 deposits were observed in adjacent Co_4N nanorod surfaces for all discharged Co_4N/CNF electrodes with different discharge current densities (Figures 4b and S14), implying the surface-mediated growth of Li_2O_2 was dominant. Those films were clearly removed after charge process without any noticeable deformation in the morphologies of brush-like Co_4N nanorods.

In TEM images (Figure 4c,d), Co_4N nanorods were clearly covered with Li_2O_2 layers. It is also noteworthy that the thickness of Li_2O_2 is about 30−60 nm, which is over the limitation of hole tunneling, suggests the contribution of polaronic transport in bulk L_2O_2 with improved ionic and electronic conductivity.[51] In the scanning TEM (STEM) image and electron energy loss spectroscopy (EELS) spectra (Figure 4e,f), the broad Li−K edge centered at 61 eV was clearly observed at around nanorods regions (marked as 1, 2), which can be ascribed to the Li_2O_2 formed along with the surface of Co_4N nanorods.[52,53]

The contribution of Co_4N to the formation and decomposition of reaction products was further verified by XRD and XPS results. The XRD patterns obtained at discharged Co_4N/CNF and CNF electrodes revealed that Li_2O_2 (marked as *) and $LiOH$ (marked as +) were formed (Figure 4g,h). Both Li_2O_2 and $LiOH$ have been reported to form on discharge in the cell,[31,54,55] but, the detection of $LiOH$ was attributed to the
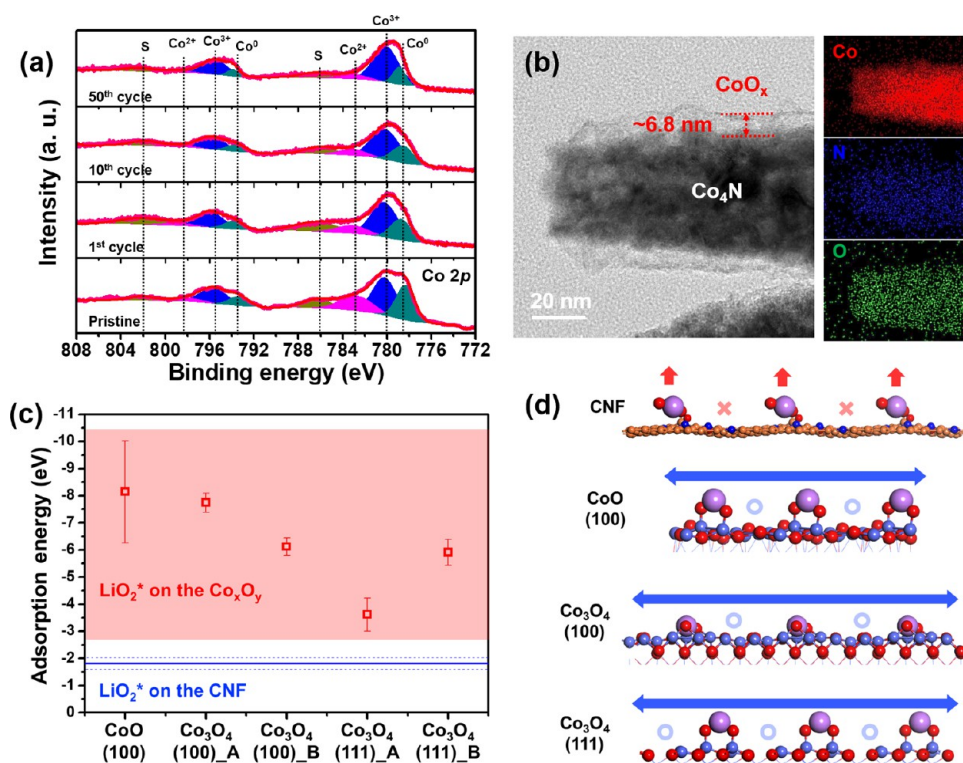
Figure 5. (a) *Ex situ* XPS spectra (Co 2p region) of Co_4N/CNF electrodes with increasing cycle numbers in $Li-O_2$ cells; (b) TEM image and corresponding EDS elemental mapping of Co_4N/CNF electrodes after 10 cycles; (c) DFT calculation results for LiO_2 adsorption energies on CNF and CoO_x layers at Co_4N/CNF; and (d) schematic illustration of LiO_2 adsorption and growth directions on CNF and CoO_x layers at Co_4N surface. Color code: carbon (orange), oxygen (red), nitrogen (blue), lithium (purple), and cobalt (sky blue).

rapid reaction of Li_2O_2 and moisture in the air before/during the measurement. For recharged Co_4N/CNF, the patterns of discharge products disappeared in a reversible manner. The Li 1s and C 1s peak changes in the XPS spectra also support the reversible discharge and recharge process on Co_4N/CNF (Figure 4i,j). However, the Li_2CO_3 peaks (marked as ◇) were observed in recharged CNF electrode (Figure 4h). In Li 1s region, Li_2CO_3 (55.4 eV), Li_2O_2 (54.7 eV), and Li_2O (53.6 eV) peaks were identified in discharged CNF electrode, and the majority of Li_2CO_3 and partial Li_2O_2 peaks were still existed after charge process (Figure 4k).[6] Further evidence for the formation of carbonates (CO_3^{2-}) was observed from C 1s region (Figure 4l), which can be assigned to Li_2CO_3 or lithium alkyl carbonates ($LiRCO_3$, R = alkyl) mainly derived from the incomplete oxidation of Li_2O_2 at the defective carbons or decomposition of electrolyte defective carbons or decomposition of electrolyte.[56] The increase in cell impedance after initial cycle is due to these insulating residues (Figure S15), resulting in high charge potentials of pristine CNF electrode. Although little Li_2CO_3 and CO_3^{2-} peaks were detected after 50 cycles on Co_4N/CNF electrode (Figure S16), the peak intensities were even lower than those of CNF electrode after initial cycling.

To give insights into OER behaviors of $Li-O_2$ cells, *in situ* gas analysis was carried out using a custom-built OEMS system for Co_4N/CNF and CNF electrodes, respectively.[57] During the first charging, both Co_4N/CNF and CNF electrodes showed O_2 gas evolution (Figure S17a,b). For CNF, significant CO_2 evolution was observed after 60% depth of charge (DOC), resulted from the decomposition of carbonate side products accumulated on CNF during discharge and/or the parasitic oxidative reaction involving electrolyte degradation. On the

other hand, there was negligible detection of CO_2 for Co_4N/CNF. Considering insignificant deposit of side products after the first charging (Figure 4) along with OEMS result, we confirmed that trivial side reactions in Co_4N/CNF occurred less compared with CNF. It may be attributed to chemical reaction of O_2 gas with the electrode of Co_4N and formation of surficial oxide layer. After repeated cycling, CO_2 gas evolution was also detected at 50% DOC from Co_4N/CNF electrode (fifth cycling, Figure S17c,d). One of the most plausible reasons for side reactions is probably due to the decomposition of electrolyte solution.

We further investigated the chemical changes of surface layers of Co_4N/CNF electrodes through *ex situ* XPS and TEM analysis (Figure 5). As the cycle number increased from 1 to 50, Co^0 bonds (778.4 eV) gradually decreased whereas Co^{3+} bonds (780.1 eV) increased in Co 2p region (Figure 5a). In consideration of the detection depth of X-ray beam (<12 nm), the chemical composition of outermost Co_4N has been changed during the repeated cycling. As shown in TEM image and EDS elemental maps in Figure 5b, it can be deduced that oxidized surficial layer was formed on Co_4N nanorods after cycling, which was also supported by the low O_2 evolution rate on Co_4N/CNF electrode at charging process (Figure S17). Based on these analytical results and previous literatures,[25] we concluded that the thin layer would be composed of oxidized cobalt species (CoO_x; CoO or Co_3O_4) with poor crystallinity. It is noteworthy that no severe structural deformation of Co_4N nanorods was found even after 50 cycles and the thickness of oxidized layer was not excessively extended (<10 nm) (Figure S18), suggesting the catalytic activities of cathode are well maintained for long cycles. Nazar's group recently reported that metal carbides or nitrides based air cathode materials have
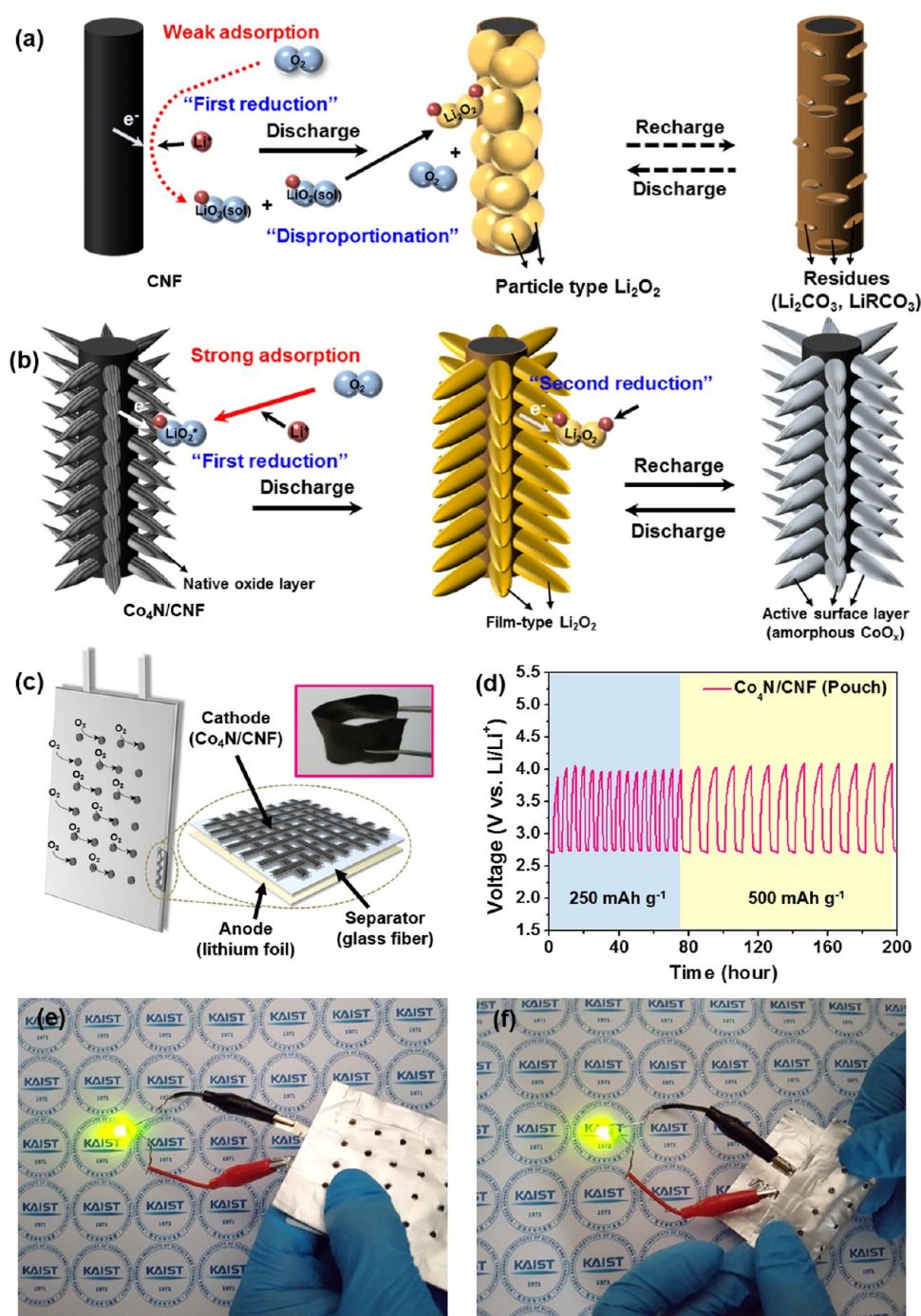
Figure 6. Proposed reaction mechanism of Li−O₂ cells with (a) CNF and (b) Co₄N/CNF electrode; (c) schematic images of flexible Li−O₂ battery using Co₄N/CNF electrode (inset); (d) voltage profile of flexible Li−O₂ batteries with different capacity restriction; and photograph images of the LED turned on with the fabricated flexible Li−O₂ batteries with (e) planar and (f) 180° bent conditions. The permission to use the logo in print or digital formats was granted from KAIST.

always suffered from the electrochemical oxidation especially during charge reaction at high OER potential.[29] They proposed TiC as a cathode material whose surface is densely covered by ultrathin TiO_2 layer (<2 nm) passivating bulk oxidation during cycling. In particular, they emphasized that the cathode surface should be designed to inhibit excessive oxidation (leading to an insulating oxide) and/or be concealed by conductive oxide layers. In this work, the amorphous CoO_x layer with less than 10 nm thickness stably passivated the metallic Co_4N center under such a harsh oxidative condition, which is certainly

confirmed by reliable cycling performance of Li−O₂ cells. Moreover, different from the insulating and catalytically inactive TiO_2, the thin CoO_x skin layer could be beneficial for the fast charge transportation into the Co_4N cores and the improved catalytic reaction during the cell operations.

DFT Calculations and Proposed Mechanism. To clarify the growth mechanism of Li_2O_2 during discharging cells, we adopted a density functional theory (DFT) calculation for evaluating the adsorption energy of reaction intermediate, LiO_2*.[48] As displayed in Figure S19, we simulated turbostratic

CNF structure with ~3 and ~5 at% O and N dopants, respectively (Figure S3d), whose calculated interlayer distance (~3.306 Å) was almost same with our TEM observation (~3.38 Å, Figure S5). The outermost layer of Co_4N/CNF was identified as the amorphous CoO_x, which was directly involved in the surface redox reaction as active sites. So, we modeled five representative CoO_x structures with different surface terminations for Co_4N/CNF: CoO (100), Co_3O_4 (100)_A, B, and Co_3O_4 (111)_A, B (Figure S20).

As shown in Figure 5c and Table S4, the LiO_2 adsorption energy on the turbostratic CNF (−1.816 eV) was much weaker than that on cobalt oxides (marked as pink area, −3.613 ~ −8.145 eV). Generally, the weak LiO_2 adsorption energy implies that adsorbed LiO_2 radicals are easily solvated in the electrolyte and they tend to be particle-type Li_2O_2, while strongly bound LiO_2 becomes film-type Li_2O_2 on the electrode surface.[46,48] This is clearly identical to our postulation from the CVs and *ex situ* observation. It should be also noted that only one oxygen of LiO_2 is participated in the chemical bonding especially at the dopant sites in CNF, and LiO_2 hardly bound on the perfectly coordinated sp^2 carbon surface due to the low adsorption energy (−0.286 eV), leading to uneven growth of Li_2O_2 as described in Figure 5d. On the other hand, two oxygen atoms of LiO_2 were simultaneously involved in strong chemical bonding at any Co−Co bridging sites, so Li_2O_2 could be uniformly deposited on the oxidized layer on Co_4N nanorods. To support this claim, we also investigated the formation and decomposition of Li_2O_2 on CoO_x/CNF electrode. As shown in Figure S21, the film-like Li_2O_2 growth was also observed after discharge process due to the high affinity of LiO_2 radicals on the CoO_x surface. However, the inherent low electronic conductivity of CoO_x without Co_4N core retarded the internal charge transfer during repeated cell operations, exhibiting worse performance than the cell using Co_4N/CNF electrode (Figure S12).

From these experimental and computational results, we proposed the plausible reaction mechanisms of the CNF and Co_4N/CNF cathodes during discharge and charge in Li−O_2 cells (Figure 6a,b). In the case of CNF cathode, initially reduced LiO_2 radical was weakly pulled to CNF surface and easily solvated. So, particle-type Li_2O_2 is mainly formed on discharge followed by disproportionation reaction. The particle-type Li_2O_2 disappeared after recharge process, but residues (Li_2CO_3 and $LiRCO_3$) obviously remained on CNF surface as evidenced by SEM and XPS. These residues can gradually deactivate the reaction sites and degrade the cell performance. By contrast, LiO_2 radicals were intimately bound through first reduction step due to the strong LiO_2 adsorption energy and stabilized to form film-type Li_2O_2 on the slightly oxidized Co_4N surfaces via further reduction step. Although lithium carbonates were also formed on Co_4N/CNF after several cycles (Figures S16, S17), Co_4N could efficiently decompose these side products as well as Li_2O_2 with low charge overpotentials (<4.0 V_{Li}), allowing the repeatable cycling.

At another point of view, the contamination of the cell by H_2O or CO_2 from the air would be unavoidable parts for real "Li−air" battery operation, and those are also responsible for the formation of LiOH or Li_2CO_3, respectively.[58] For these reasons, the efficient mediation of side reaction products is very important for the stable operation of Li−air cells. In order to demonstrate the practical use of Co_4N/CNF as air cathode in Li−air battery, we fabricated air permeable pouch-type cells consisted of Co_4N/CNF cathode, a glass fiber separator, and a lithium foil anode (Figure 6c).[59] The Li−air cell using a Co_4N/CNF cathode showed stable cycling performance upon different limited capacities (250 and 500 mAh g^{-1}) for over 200 h without severe polarizations (Figure 6d). Furthermore, the Li−air cell successfully powered a commercial green light-emitting diode (LED), regardless of whether the battery was in planar or various bent state (up to the bending angle of 180°), as shown in Figures 6e,f and S22. These comprehensive results reveal that our Co_4N/CNF membrane has sufficient electrochemical and mechanical stability as an air cathode even under bending strain in the Li−air battery.

CONCLUSION

In summary, we fabricated a free-standing Co_4N/CNF catalyst-current collector integrated electrode that overcomes the challenge of air electrodes in nonaqueous Li−O_2 batteries. When brush-like Co_4N nanorod anchored CNF paper was directly employed as air cathode, the Li−O_2 cell showed high capacity (11.9 mAh cm^{-2}) and enhanced cycling capability (>177 cycles). The superior performance of Co_4N/CNF is attributed to its suitable design and tailored properties, such as (i) improved charge transfer due to the direct electrical contact between metallic catalysts (Co_4N with 50 nm diameter and 2−5 μm length) and N-doped CNF without the use of binder, (ii) numerous active sites of densely formed Co_4N nanorods accommodating solid reaction products (Li_2O_2), and (iii) the reliable and active surface layer (amorphous CoO_x film) on Co_4N facilitating ORR/OER with low overpotentials. The in-depth analysis and insights from this work can offer a better understanding about the importance of rational electrode design and a substantial progress in this field. Furthermore, we confident that the electrode construction concept and method can be widely used in other electrocatalysis fields such as fuel cells and metal-air batteries.

METHODS

Synthesis of Carbon Nanofiber (CNF) Paper. Polyacrylonitrile (PAN, Mw = 150 000 g mol^{-1}), N,N-dimethylformamide (DMF), cobalt(II) nitrate hexahydrate ($Co(NO_3)_2 \cdot 6H_2O$), urea ($CO(NH_2)_2$), ammonium fluoride (NH_4F) were purchased from Sigma-Aldrich and they were used without further purification process. To synthesize electrospun carbon nanofiber (CNF) paper, 1 g of PAN was dissolved in 6 g of DMF under vigorous stirring at 80 °C for 6 h. The PAN/DMF solution was transferred into the syringe, and the 25-gauge needle was capped on the syringe tip. High voltage of 12.5 kV was applied between the needle and the stainless steel collector, which were separated with a distance of 15 cm, then the elongated PAN was continuously fed from the needle to collector with a feeding rate of 15 μL min^{-1}. The electrospun PAN fibers were stabilized first at 250 °C for 2 h in air followed by carbonization at 900 °C for 2 h in Ar-filled tube furnace. The resultant sample was designated as CNF.

Preparation of Co_4N/CNF and CoO_x/CNF Membranes. The Co_4N/CNF (Co_4N nanorods anchored CNF) was prepared using a simple hydrothermal method and subsequent nitridation process.[25] In order to give hydrophilic nature, a piece of CNF (2 cm × 2 cm) was placed in 70% concentrated nitric acid (HNO_3) at 80 °C for 2 h. Acid treated CNF was washed with DI water for several times and then dried in a convection oven at 50 °C. Back side of cleaned CNF was masked with polyimide (PI) tape for preserving the electrical contact in Li−O_2 cell. Next, 0.291 g of $Co(NO_3)_2 \cdot 6H_2O$, 0.093 g of NH_4F, and 0.3 g of urea were dissolved in 20 mL of DI water, and then cleaned CNF was soaked in the mixed solution under stirring at 100 rpm for over 2 h. The mixed solution and CNF were transferred to a 50 mL Teflon-lined autoclave and kept at 120 °C for 6 h (5 °C min^{-1}). After cooling down to room temperature, the cobalt fluoride hydroxide

coated CNF (Co(OH)F/CNF) was taken out and rinsed with DI water and EtOH for several times, and dried in a convection oven at 50 °C. Finally, the Co(OH)F/CNF was calcined at 550 °C for 2 h (5 °C min^{-1}) in a Ar-filled tube furnace with ammonia gas (NH$_3$) at a flow rate of 100 sccm. The obtained product was designated as Co$_4$N/CNF. A mass loading of Co$_4$N on CNF was 0.9 mg cm^{-2} which comes to 1.8 mg cm^{-2} of total Co$_4$N/CNF mass, and a total thickness of Co$_4$N/CNF paper was 100 μm. As a comparative sample, CoO$_x$/CNF was obtained at the same calcination condition only with Ar atmosphere without NH$_3$ gas flow.

Material Characterization. The microstructures of the prepared samples were observed using scanning electron microscope (Philips, USA) and Tecnai TF30 S-Twin transmission electron microscope (FEI Company, USA). The crystalline structure of the samples was analyzed by using powder X-ray diffractometer (D/MAX-2500, RIGAKU Co., Japan) and the surface chemical state was investigated by using X-ray photoelectron spectroscopy (Thermo VG Scientific Co., UK). The properties of carbon materials were analyzed by using Raman spectroscopy (Horiba Jobin Yvon, France). Infrared spectrum of the samples was measured by using Fourier Transform Infrared Spectrometer (Nicolet iS50, Thermo Fisher Scientific Inc., Korea).

Assembly of Li–O$_2$ Batteries and Electrochemical Cell Tests. A Swagelok-type Li–O$_2$ cell was assembled in an Ar-filled glovebox using a lithium foil anode, glass fiber separator (Whatman), Co$_4$N/CNF cathode, gas diffusion layer (GDL 10 BC, CNL Energy), and 1 M lithium bis(trifluoromethylsulfonyl)imide (LiTFSI) in tetra-(ethylene) glycol dimethyl ether (TEGDME) electrolyte. The active cathode area was 1.09 cm^2 (diameter of 11.8 mm). After the assembled cell was taken out of the glovebox, the cell was subjected to the O$_2$-filled pipeline (760 Torr) in a thermostat chamber, and kept for 3 h to saturate O$_2$ in the cell before testing. The pouch-type Li–air battery was also assembled in Ar-filled glovebox using lithium foil anode, glass fiber separator, and Co$_4$N/CNF cathode (2 cm × 2 cm), which are attached onto the one side of pouch by polyimide (PI) tape and 1 M LiTFSI in TEGDME was used as electrolyte. The other side of pouch facing the air cathode has 1 mm sized 24 holes at an interval of 8 mm for air penetration. Polytetrafluoroethylene (PTFE) membrane was attached onto the inner side for minimizing evaporation of liquid electrolyte and permeation of moisture from the air. Finally, the both sides of pouch were thermally pressed for packing the cell. The cell performance was measured using a battery testing setup (series 4000 system, Maccor, USA) at room temperature. Cyclic voltammetry (CV) and electrochemical impedance spectroscopy (EIS) were measured by potentiostat (ZIVE SP1, ZIVE LAB, Korea).

Gas Evolution Profile Measurement. The Li–O$_2$ cell (Tomcell, Japan) assembled in an Ar-filled glovebox was connected to custom-built Online Electrochemical Mass Spectroscopy (OEMS) system and discharge process was carried out after O$_2$ gas filling. The cell was purged with Ar gas after discharging process and gas evolution was monitored at 25 °C during recharging process. The evolving gas was accumulated for every 30 min and analyzed using mass spectrometer (RGA200, Stanford Research Systems, USA). The pressure change of Li–O$_2$ cell was concomitantly measured using high precision pressure transducer (MMA030V5P3A6T3A5CE, Omega Engineering, USA) for quantitative gas analysis. The detailed description of OEMS setup and experimental process can be found in our previous report.[57]

Computational Details. For the entire calculation performed in this study, we used generalized gradient approximation (GGA)-level spin-polarized density functional theory (DFT) calculations with plane-wave based Vienna ab initio simulation package (VASP) code.[60] The BEEF-vdw exchange correlation functional[61] was utilized to describe surface chemistry and molecular adsorption on the modified graphene and metal oxide systems due to its high accuracy about adsorption property and consideration of van der Waals interactions. Cut-off energy was set to 500 eV, k-point sampling was chosen with 3 × 3 × 1, and convergence criteria for electronic structures and atomic geometry optimization were 10^{-5} eV and 0.01 eV Å^{-1}, respectively. We designed turbostratic CNF from the successful finding regarding commensuration cell of turbostratic graphene by S. Shallcross and co-workers.[62] We expanded it to 2 × 2 supercell, which includes

elemental vacancies, and doped N and O atoms to match with experimental results.

From the XPS analysis in Figure 5a, we modeled five different kinds of cobalt oxide systems: CoO (100), Co$_3$O$_4$ (100)_A, B, and Co$_3$O$_4$ (111)_A, B. CoO (100) slab was used with 2 × 2 supercell and had four repeating layers (one repeating layer = one atomic layer) with two fixed repeating bottom layers in their bulk positions, Co$_3$O$_4$ (100) was used with 2 × 1 supercell and had three repeating layers (one repeating layer = two atomic layers) with two fixed repeating bottom layers, and Co$_3$O$_4$ (111) was used with 2 × 2 supercell and had two repeating layers (one repeating layer = six atomic layers) with one fixed repeating bottom layer. Every substrate systems are centered between 10 Å vacuums including CNF, which is enough space to avoid self-interaction due to the periodic boundary condition. The adsorption energy of LiO$_2$ (ΔE_{ads}) was calculated as followed equation:

$$\Delta E_{ads} = E_{Substrate+LiO_2} - (E_{Substrate} + E_{LiO_2})$$

where $E_{Substrate+LiO_2}$ is the total energy of LiO$_2$ adsorbed system, $E_{Substrate}$ is the total energy of substrate before the adsorption, and E_{LiO_2} stands for the total energy of isolated LiO$_2$ itself. More negative value of adsorption energy represents greater exothermic and stronger chemisorption.

ASSOCIATED CONTENT

Ⓢ Supporting Information

The Supporting Information is available free of charge on the ACS Publications website at DOI: 10.1021/acsnano.7b03794.

Tables and additional Figures including SEM, TEM, XPS, and XRD data, electrical properties, electrochemical results, OEMS data, schematic representations for DFT calculations, and photograph images (PDF)

AUTHOR INFORMATION

Corresponding Author
*E-mail: idkim@kaist.ac.kr.

ORCID Ⓘ
Hyuk Mo Lee: 0000-0003-4556-6692
Il-Doo Kim: 0000-0002-9970-2218

Notes
The authors declare no competing financial interest.

ACKNOWLEDGMENTS

REFERENCES

(1) Armand, M.; Tarascon, J. M. Building Better Batteries. *Nature* **2008**, *451*, 652−657.
(2) Bruce, P. G.; Freunberger, S. A.; Hardwick, L. J.; Tarascon, J. M. Li−O$_2$ and Li−S Batteries with High Energy Storage. *Nat. Mater.* **2011**, *11*, 19−29.

(3) Kraytsberg, A.; Ein-Eli, Y. Review on Li−Air Batteries—Opportunities, Limitations and Perspective. *J. Power Sources* **2011**, *196*, 886−893.

(4) Lu, Y.-C.; Gallant, B. M.; Kwabi, D. G.; Harding, J. R.; Mitchell, R. R.; Whittingham, M. S.; Shao-Horn, Y. Lithium−Oxygen Batteries: Bridging Mechanistic Understanding and Battery Performance. *Energy Environ. Sci.* **2013**, *6*, 750−768.

(5) Yoon, K. R.; Kim, D. S.; Ryu, W. H.; Song, S. H.; Youn, D. Y.; Jung, J. W.; Jeon, S.; Park, Y. J.; Kim, I. D. Tailored Combination of Low Dimensional Catalysts for Efficient Oxygen Reduction and Evolution in Li−O₂ Batteries. *ChemSusChem* **2016**, *9*, 2080−2088.

(6) Yoon, K. R.; Lee, G. Y.; Jung, J. W.; Kim, N. H.; Kim, S. O.; Kim, I. D. One-Dimensional RuO₂/Mn₂O₃ Hollow Architectures as Efficient Bifunctional Catalysts for Lithium−Oxygen Batteries. *Nano Lett.* **2016**, *16*, 2076−2083.

(7) Ryu, W. H.; Yoon, T. H.; Song, S. H.; Jeon, S.; Park, Y. J.; Kim, I. D. Bifunctional Composite Catalysts Using Co₃O₄ Nanofibers Immobilized on Nonoxidized Graphene Nanoflakes for High-Capacity and Long-Cycle Li−O₂ Batteries. *Nano Lett.* **2013**, *13*, 4190−4197.

(8) Kim, D. S.; Park, Y. J. Ketjen Black/Co₃O₄ Nanocomposite Prepared Using Polydopamine Pre-Coating Layer as a Reaction Agent: Effective Catalyst for Air Electrodes of Li/Air Batteries. *J. Alloys Compd.* **2013**, *575*, 319−325.

(9) Yoon, T. H.; Park, Y. J. Polydopamine-Assisted Carbon Nanotubes/Co₃O₄ Composites for Rechargeable Li-Air Batteries. *J. Power Sources* **2013**, *244*, 344−353.

(10) Xiao, J.; Kuang, Q.; Yang, S.; Xiao, F.; Wang, S.; Guo, L. Surface Structure Dependent Electrocatalytic Activity of Co₃O₄ Anchored on Graphene Sheets toward Oxygen Reduction Reaction. *Sci. Rep.* **2013**, *3*, 2300.

(11) Lee, H.; Kim, Y. J.; Lee, D. J.; Song, J.; Lee, Y. M.; Kim, H. T.; Park, J. K. Directly Grown Co₃O₄ Nanowire Arrays on Ni-Foam: Structural Effects of Carbon-Free and Binder-Free Cathodes for Lithium−Oxygen Batteries. *J. Mater. Chem. A* **2014**, *2*, 11891−11898.

(12) Higashi, M.; Domen, K.; Abe, R. Fabrication of Efficient TaON and Ta₃N₅ Photoanodes for Water Splitting under Visible Light Irradiation. *Energy Environ. Sci.* **2011**, *4*, 4138−4147.

(13) Zukalova, M.; Prochazka, J.; Bastl, Z.; Duchoslav, J.; Rubacek, L.; Havlicek, D.; Kavan, L. Facile Conversion of Electrospun TiO₂ into Titanium Nitride/Oxynitride Fibers. *Chem. Mater.* **2010**, *22*, 4045−4055.

(14) Abe, R.; Higashi, M.; Domen, K. Facile Fabrication of an Efficient Oxynitride TaON Photoanode for Overall Water Splitting into H₂ and O₂ under Visible Light Irradiation. *J. Am. Chem. Soc.* **2010**, *132*, 11828−11829.

(15) Li, F.; Ohnishi, R.; Yamada, Y.; Kubota, J.; Domen, K.; Yamada, A.; Zhou, H. Carbon Supported TiN Nanoparticles: An Efficient Bifunctional Catalyst for Non-Aqueous Li−O₂ Batteries. *Chem. Commun.* **2013**, *49*, 1175−1177.

(16) Fischer, A.; Jun, Y.; Thomas, A.; Antonietti, M. Synthesis of High-Surface-Area TiN/Carbon Composite Materials with Hierarchical Porosity via "Reactive Templating. *Chem. Mater.* **2008**, *20*, 7383−7389.

(17) Dong, S.; Chen, X.; Zhang, K.; Gu, L.; Zhang, L.; Zhou, X.; Li, L.; Liu, Z.; Han, P.; Xu, H.; Yao, J.; Zhang, C.; Zhang, X.; Shang, C.; Cui, G.; Chen, L. Molybdenum Nitride Based Hybrid Cathode for Rechargeable Lithium−O₂ Batteries. *Chem. Commun.* **2011**, *47*, 11291−11293.

(18) Shalom, M.; Ressnig, D.; Yang, X.; Clavel, G.; Fellinger, T. P.; Antonietti, M. Nickel Nitride as an Efficient Electrocatalyst for Water Splitting. *J. Mater. Chem. A* **2015**, *3*, 8171−8177.

(19) Meng, F.; Zhong, H.; Bao, D.; Yan, J.; Zhang, X. In Situ Coupling of Strung Co₄N and Intertwined N−C Fibers toward Free-Standing Bifunctional Cathode for Robust, Efficient, and Flexible Zn−Air Batteries. *J. Am. Chem. Soc.* **2016**, *138*, 10226−10231−10231.

(20) Zhong, X.; Liu, L.; Jiang, Y.; Wang, X.; Wang, L.; Zhuang, G.; Li, X.; Mei, D.; Wang, J.-g. D.; Su, S. Synergistic Effect of Nitrogen in Cobalt Nitride and Nitrogen-Doped Hollow Carbon Spheres for the Oxygen Reduction Reaction. *ChemCatChem* **2015**, *7*, 1826−1832.

(21) Jiang, M.; Li, Y.; Lu, Z.; Sun, X.; Duan, X. Binary Nickel−Iron Nitride Nanoarrays as Bifunctional Electrocatalysts for Overall Water Splitting. *Inorg. Chem. Front.* **2016**, *3*, 630−634.

(22) Zhang, K.; Zhang, L.; Chen, X.; He, X.; Wang, X.; Dong, S.; Han, P.; Zhang, C.; Wang, S.; Gu, L.; Cui, G. Mesoporous Cobalt Molybdenum Nitride: A Highly Active Bifunctional Electrocatalyst and Its Application in Lithium−O₂ Batteries. *J. Phys. Chem. C* **2013**, *117*, 858−865.

(23) Cao, B.; Veith, G. M.; Neuefeind, J. C.; Adzic, R. R.; Khalifah, P. G. Mixed Close-Packed Cobalt Molybdenum Nitrides as Non-Noble Metal Electrocatalysts for the Hydrogen Evolution Reaction. *J. Am. Chem. Soc.* **2013**, *135*, 19186−19192.

(24) Chen, P.; Xu, K.; Tong, Y.; Li, X.; Tao, S.; Fang, Z.; Chu, W.; Wu, X.; Wu, C. Cobalt Nitrides as a Class of Metallic Electrocatalysts for the Oxygen Evolution Reaction. *Inorg. Chem. Front.* **2016**, *3*, 236−242.

(25) Chen, P.; Xu, K.; Fang, Z.; Tong, Y.; Wu, J.; Lu, X.; Peng, X.; Ding, H.; Wu, C.; Xie, Y. Metallic Co₄N Porous Nanowire Arrays Activated by Surface Oxidation as Electrocatalysts for the Oxygen Evolution Reaction. *Angew. Chem., Int. Ed.* **2015**, *54*, 14710−14714.

(26) Peng, S.; Li, L.; Hu, Y.; Srinivasan, M.; Cheng, F.; Chen, J.; Ramakrishna, S. Fabrication of Spinel One-Dimensional Architectures by Single-Spinneret Electrospinning for Energy Storage Applications. *ACS Nano* **2015**, *9*, 1945−1954.

(27) Liu, Q. C.; Xu, J. J.; Yuan, S.; Chang, Z. W.; Xu, D.; Yin, Y. B.; Li, L.; Zhong, H. X.; Jiang, Y. S.; Yan, J. M.; Zhang, X. B. Artificial Protection Film on Lithium Metal Anode toward Long-Cycle-Life Lithium−Oxygen Batteries. *Adv. Mater.* **2015**, *27*, 5241−5247.

(28) Wu, D. F.; Guo, Z. Y.; Yin, X. B.; Pang, Q. Q.; Tu, B. B.; Zhang, L. J.; Wang, Y. G.; Li, Q. W. Metal−Organic Frameworks as Cathode Materials for Li−O₂ Batteries. *Adv. Mater.* **2014**, *26*, 3258−3262.

(29) Adams, B. D.; Black, R.; Radtke, C.; Williams, Z.; Mehdi, B. L.; Browning, N. D.; Nazar, L. F. The Importance of Nanometric Passivating Films on Cathodes for Li-Air Batteries. *ACS Nano* **2014**, *8*, 12483−12493.

(30) Liu, Q.-c.; Xu, J.-j.; Chang, Z.-w.; Xu, D.; Yin, Y.-b.; Yang, X.-y.; Liu, T.; Jiang, Y.-s.; Yan, J.-m.; Zhang, X.-b. Growth of Ru-Modified Co₃O₄ Nanosheets on Carbon Textiles toward Flexible and Efficient Cathodes for Flexible Li−O₂ Batteries. *Part. Part. Syst. Charact.* **2016**, *33*, 500−505.

(31) Black, R.; Oh, S. H.; Lee, J. H.; Yim, T.; Adams, B.; Nazar, L. F. Screening for Superoxide Reactivity in Li-O₂ Batteries: Effect on Li₂O₂/LiOH Crystallization. *J. Am. Chem. Soc.* **2012**, *134*, 2902−2905.

(32) Tan, P.; Shyy, W.; Zhao, T. S.; Zhu, X. B.; Wei, Z. H. A RuO₂ Nanoparticle-Decorated Buckypaper Cathode for Non-Aqueous Lithium−Oxygen Batteries. *J. Mater. Chem. A* **2015**, *3*, 19042−19049.

(33) Yoon, K. R.; Ko, J. W.; Youn, D. Y.; Park, C. B.; Kim, I. D. Synthesis of Ni-based Co-Catalyst Functionalized W: BiVO₄ Nano-fibers for Solar Water Oxidation. *Green Chem.* **2016**, *18*, 944−950.

(34) Rahaman, M. S. A.; Ismail, A. F.; Mustafa, A. A Review of Heat Treatment on Polyacrylonitrile Fiber. *Polym. Degrad. Stab.* **2007**, *92*, 1421−1432.

(35) Zhang, B.; Kang, F.; Tarascon, J. M.; Kim, J. K. Recent Advances in Electrospun Carbon Nanofibers and Their Application in Electrochemical Energy Storage. *Prog. Mater. Sci.* **2016**, *76*, 319−380.

(36) Oda, K.; Yoshio, T.; Oda, K. Preparation of Co-N Films by Rf-Sputtering. *J. Mater. Sci.* **1987**, *22*, 2729−2733.

(37) Ferrari, A. C. Raman Spectroscopy of Graphene and Graphite: Disorder, Electron−Phonon Coupling, Doping and Nonadiabatic Effects. *Solid State Commun.* **2007**, *143*, 47−57.

(38) Kornienko, N.; Resasco, J.; Becknell, N.; Jiang, C. M.; Liu, Y. S.; Nie, K.; Sun, X.; Guo, J.; Leone, S. R.; Yang, P. *Operando* Spectroscopic Analysis of an Amorphous Cobalt Sulfide Hydrogen Evolution Electrocatalyst. *J. Am. Chem. Soc.* **2015**, *137*, 7448−7455.

(39) Yan, C.; Chen, G.; Zhou, X.; Sun, J.; Lv, C. Template-Based Engineering of Carbon-Doped Co₃O₄ Hollow Nanofibers as Anode Materials for Lithium-Ion Batteries. *Adv. Funct. Mater.* **2016**, *26*, 1428−1436.

(40) Kumar, B.; Asadi, M.; Pisasale, D.; Sinha-Ray, S.; Rosen, B. A.; Haasch, R.; Abiade, J.; Yarin, A. L.; Salehi-Khojin, A. Renewable and Metal-Free Carbon Nanofibre Catalysts for Carbon Dioxide Reduction. *Nat. Commun.* **2013**, *4*, 2819.

(41) Yu, S.; Kim, J.; Yoon, K. R.; Jung, J. W.; Oh, J.; Kim, I. D. Rational Design of Efficient Electrocatalysts for Hydrogen Evolution Reaction: Single Layers of WS_2 Nanoplates Anchored to Hollow Nitrogen-Doped Carbon Nanofiber. *ACS Appl. Mater. Interfaces* **2015**, *7*, 28116−28121.

(42) Gong, K.; Du, F.; Xia, Z.; Durstock, M.; Dai, L. Nitrogen-Doped Carbon Nanotube Arrays with High Electrocatalytic Activity for Oxygen Reduction. *Science* **2009**, *323*, 760−764.

(43) Geng, D.; Chen, Y.; Chen, Y.; Li, Y.; Li, R.; Sun, X.; Ye, S.; Knights, S. High Oxygen-Reduction Activity and Durability of Nitrogen-Doped Graphene. *Energy Environ. Sci.* **2011**, *4*, 760−764.

(44) Tang, Y.; Allen, B. L.; Kauffman, D. R.; Star, A. Electrocatalytic Activity of Nitrogen-Doped Carbon Nanotube Cups. *J. Am. Chem. Soc.* **2009**, *131*, 13200−13201.

(45) Mohimi, E.; Trinh, B. B.; Babar, S.; Girolami, G. S.; Abelson, J. R. Chemical Vapor Deposition of Mn_xN_y Films from Bis(2,2,6,6-tetramethylpiperidido)manganese(II) and Ammonia. *J. Vac. Sci. Technol., A* **2016**, *34*, 060603−13201.

(46) Aurbach, D.; McCloskey, B. D.; Nazar, L. F.; Bruce, P. G. Advances in Understanding Mechanisms Underpinning Lithium−Air Batteries. Nat. *Energy* **2016**, *1*, 16128.

(47) Aetukuri, N. B.; McCloskey, B. D.; Garcia, J. M.; Krupp, L. E.; Viswanathan, V.; Luntz, A. C. Solvating Additives Drive Solution-Mediated Electrochemistry and Enhance Toroid Growth in Non-Aqueous Li−O_2 Batteries. *Nat. Chem.* **2014**, *7*, 50−56.

(48) Xu, J. J.; Chang, Z. W.; Wang, Y.; Liu, D. P.; Zhang, Y.; Zhang, X. B. Cathode Surface-Induced, Solvation-Mediated, Micrometer-Sized Li_2O_2 Cycling for Li−O_2 Batteries. *Adv. Mater.* **2016**, *28*, 9620−9628.

(49) Lu, Y. C.; Shao-Horn, Y. Probing the Reaction Kinetics of the Charge Reactions of Nonaqueous Li−O_2 Batteries. *J. Phys. Chem. Lett.* **2013**, *4*, 93−99.

(50) Ottakam Thotiyl, M. M.; Freunberger, S. A.; Peng, Z.; Bruce, P. G. The Carbon Electrode in Nonaqueous Li−O_2 Cells. *J. Am. Chem. Soc.* **2013**, *135*, 494−500.

(51) Radin, M. D.; Monroe, C. W.; Siegel, D. J. Impact of Space-Charge Layers on Sudden Death in Li/O_2 Batteries. *J. Phys. Chem. Lett.* **2015**, *6*, 3017−3022.

(52) Xiao, D.; Dong, S.; Guan, J.; Gu, L.; Li, S.; Zhao, N.; Shang, C.; Yang, Z.; Zheng, H.; Chen, C.; Xiao, R.; Hu, Y. S.; Li, H.; Cui, G.; Chen, L. Direct Observation of Ordered Oxygen Defects on the Atomic Scale in Li_2O_2 for Li-O_2 Batteries. Adv. *Energy Mater.* **2015**, *5*, 1400664.

(53) Zhong, L.; Mitchell, R. R.; Liu, Y.; Gallant, B. M.; Thompson, C. V.; Huang, J. Y.; Mao, S. X.; Shao-Horn, Y. *In Situ* Transmission Electron Microscopy Observations of Electrochemical Oxidation of Li_2O_2. *Nano Lett.* **2013**, *13*, 2209−2214.

(54) Freunberger, S.; Chen, Y.; Drewett, N.; Hardwick, L.; Bardé, F.; Bruce, P. G. The Lithium-Oxygen Battery with Ether-Based Electrolytes. *Angew. Chem., Int. Ed.* **2011**, *50*, 8609−8613.

(55) Liu, T.; Leskes, M.; Yu, W.; Moore, A. J.; Zhou, L.; Bayley, P. M.; Kim, G.; Grey, C. P. Cycling Li-O_2 Batteries *via* LiOH Formation and Decomposition. *Science* **2015**, *350*, 530−533.

(56) McCloskey, B. D.; Speidel, A.; Scheffler, R.; Miller, D. C.; Viswanathan, V.; Hummelshøj, J. S.; Nørskov, J. K.; Luntz, A. C. Solvents' Critical Role in Nonaqueous Lithium-Oxygen Battery Electrochemistry. *J. Phys. Chem. Lett.* **2012**, *3*, 997−1001.

(57) Wong, R. A.; Dutta, A.; Yang, C.; Yamanaka, K.; Ohta, T.; Nakao, A.; Waki, K.; Byon, H. R. Structurally Tuning Li_2O_2 by Controlling the Surface Properties of Carbon Electrodes: Implications for Li−O_2 Batteries. *Chem. Mater.* **2016**, *28*, 8006−8015.

(58) Meini, S.; Tsiouvaras, N.; Schwenke, K. U.; Piana, M.; Beyer, H.; Lange, L.; Gasteiger, H. A. Rechargeability of Li-Air Cathodes Pre-Filled with Discharge Products Using an Ether-Based Electrolyte Solution: Implications for Cycle-Life of Li-Air Cells. *Phys. Chem. Chem. Phys.* **2013**, *15*, 11478−11493.

(59) Liu, Q. C.; Xu, J. J.; Xu, D.; Zhang, X. B. Flexible Lithium−Oxygen Battery Based on a Recoverable Cathode. *Nat. Commun.* **2015**, *6*, 7892.

(60) Kresse, G.; Furthmüller, J. Efficient Iterative Schemes for *Ab Initio* Total-Energy Calculations Using a Plane-Wave Basis Set. *Phys. Rev. B: Condens. Matter Mater. Phys.* **1996**, *54*, 11169−11186.

(61) Wellendorff, J.; Lundgaard, K. T.; Møgelhøj, A.; Petzold, V.; Landis, D. D.; Nørskov, J. K.; Bligaard, T.; Jacobsen, K. W. Density Functionals for Surface Science: Exchange-Correlation Model Development with Bayesian Error Estimation. *Phys. Rev. B: Condens. Matter Mater. Phys.* **2012**, *85*, 235149.

(62) Shallcross, S; Kandelaki, E.; Pankratov, O. A.; Sharma, S. Electronic Structure of Turbostratic Graphene. *Phys. Rev. B: Condens. Matter Mater. Phys.* **2010**, *81*, 165105.